

Constraining the Baryon Content of Cosmic Filaments Using Localized Fast Radio Bursts and DESI Imaging Data

JIAN-FENG MO,^{1,2} WEISHAN ZHU,^{1,2} QI-RUI YANG,^{1,2} YI ZHENG,^{1,2} AND LONG-LONG FENG^{1,2}

¹*School of Physics and Astronomy, Sun Yat-Sen University, Zhuhai campus, No. 2, Daxue Road
Zhuhai, Guangdong, 519082, China*

²*CSST Science Center for the Guangdong-Hong Kong-Macau Greater Bay Area, Daxue Road 2, 519082, Zhuhai, China*

ABSTRACT

Cosmic filaments are thought to host a substantial fraction of the missing baryons at redshifts $z < 2$. In this study, we constraint the baryonic content of these filaments using localized Fast Radio Bursts (FRBs). Filaments are identified from the galaxy distribution in the Dark Energy Spectroscopic Instrument (DESI) imaging surveys using the DisPerSE algorithm. We find tentative evidence ($\sim 3\sigma$ significance) for a divergence in the relationship between the dispersion measure (DM) contributed by the intergalactic medium and redshift for FRBs whose signals intersect cosmic filaments compared to those that do not, suggesting excess baryons in the filamentary structures. Assuming an isothermal β -model gas profile with $\beta = 2/3$, this discrepancy is best explained by a central baryon overdensity of $\delta_0 = 21^{+13}_{-12}$, broadly consistent with previous simulation and observational results. The inferred baryon fraction residing in filaments decreases with redshift, from approximately $0.25\text{--}0.30\Omega_b$ at $z = 0.02$ to $0.15\text{--}0.30\Omega_b$ at $z = 0.5$, and $0.03\text{--}0.04\Omega_b$ at $z = 0.8$. These estimates are likely lower bounds, particularly at $z > 0.5$, due to the limited number of identified filaments and localized FRBs at higher redshifts. We also examine various factors that may affect the statistical significance of our results. Our method offers an independent approach to tracing baryons in cosmic filaments and underscores the importance of expanding localized FRB samples and deepening galaxy surveys—key steps toward refining these estimates and addressing the missing baryon problem.

Keywords: Cosmology (343) — Large-scale structure of the universe (902) — Cosmic Web (330) — Intergalactic medium (813) — Radio transient sources (2008)

1. INTRODUCTION

According to the Λ CDM cosmology (e.g., Planck Collaboration et al. 2016), $\sim 5\%$ of the energy density in the universe are made up by baryonic matter. However, a significant portion, about 30–50%, at redshift $z < 2$ are ‘missing’ from detection for a long time (M. Persic & P. Salucci 1992; M. Fukugita et al. 1998; J. M. Shull et al. 2012; C. W. Danforth et al. 2016). Meanwhile, simulations predicted that approximately 40–60% of the baryons reside within the filamentary structures of cosmic web (R. Cen & J. P. Ostriker 1999; R. Davé et al. 2001; M. Haider et al. 2016; W. Zhu & L.-L. Feng 2017; W. Cui et al. 2018) at $z < 2$. Furthermore, simulations indicate that cosmic filaments host approximately 60–90% of the warm-hot intergalactic medium (WHIM),

which is believed to account for the majority of ‘missing’ baryons (D. Martizzi et al. 2019; T. Tuominen et al. 2021).

A variety of observational techniques have been developed to detect baryons in cosmic filaments, including X-ray emission and absorption (e.g., J. N. Bregman et al. 2009; D. Eckert et al. 2015; H. Akamatsu et al. 2017; T. Fang et al. 2002; F. Nicastro et al. 2005; M. Bonamente et al. 2016; F. Nicastro et al. 2018; J. Nevalainen et al. 2019; H. Tanimura et al. 2020b; K. Migkas et al. 2025), the thermal Sunyaev-Zel’dovich (SZ) effect (V. Bonjean et al. 2018; H. Tanimura et al. 2019; A. de Graaff et al. 2019; H. Tanimura et al. 2020a). However, the statistical significance of many of these detections remains at the $3\text{--}4\sigma$ level. In addition, several reported detections require further confirmation. Continued development of complementary observational tools is crucial for robustly identifying and quantifying the baryon content in cosmic filaments.

Fast radio bursts (FRBs) are luminous and millisecond-duration events, though their physical origin is still an open question (D. R. Lorimer et al. 2007; J. M. Cordes & S. Chatterjee 2019; B. Zhang 2023). As FRB signals propagate through ionized plasma, lower frequencies are delayed relative to higher ones—a phenomenon quantified by the dispersion measure (DM), which reflects the integrated free electron density along the line of sight (L.O.S.). M. McQuinn (2014) first proposed using the DM of FRBs to probe the universe’s missing baryons, and subsequent studies have made significant progress.

J. P. Macquart et al. (2020) analyzed the DM of seven well-localized, low-redshift FRBs and measured the cosmic baryon density as $\Omega_b h_{70} = 0.051^{+0.021}_{-0.025}$, broadly consistent with estimates from cosmic microwave background (CMB) observations (Planck Collaboration et al. 2016), albeit with large statistical uncertainties. K. B. Yang et al. 2022 used 22 localized FRBs to measure the baryon content in the universe, giving $\Omega_b = 0.049^{+0.0036}_{-0.0033}$ in 1σ confidence level. More recently, L. Connor et al. (2025) further used a larger sample of 69 localized FRBs to yield $\Omega_b h_{70} = 0.051^{+0.006}_{-0.006}$. Despite these advancements, such studies do not resolve the detailed distribution of baryons within collapsed halos and the cosmic web.

Based on cosmological hydrodynamical simulations, W. Zhu et al. (2018) demonstrated that ionized baryons in cosmic filaments contribute approximately 35–45% of the total DM of FRBs at $z < 2$. Furthermore, W. Zhu & L.-L. Feng (2021) found that the median DM contribution from foreground halos is about 30% of that from the intergalactic medium (IGM), albeit with substantially variance. More recently, several studies have reported cases where FRB signals intersect individual foreground halos, groups, walls, or filaments (e.g., S. Simha et al. 2020; K.-G. Lee et al. 2023; S. Simha et al. 2023; I. S. Khrykin et al. 2024; J. T. Faber et al. 2024; K. Shin et al. 2024). These developments make it increasingly feasible to estimate the specific DM contributions from ionized baryons in collapsed halos and cosmic web, offering a path toward constraining their detailed baryon distributions.

With the growing number of well-localized events (e.g., S. P. Tendulkar et al. 2017; K. E. Heintz et al. 2020; CHIME/FRB Collaboration et al. 2021; C. J. Law et al. 2023; J.-f. Mo et al. 2025), FRBs are becoming a powerful tool to probe baryons in cosmic filaments. At $z < 1$, filaments occupy $\sim 10\%$ of the cosmic volume, and high-redshift FRBs can intersect multiple filaments. Due to the inhomogeneous filament distribution, even FRBs at similar redshifts may traverse different

numbers of filaments, leading to variation in their extragalactic DMs. However, this signal is complicated by contributions from host galaxies, their CGM, and foreground halos (W. Zhu & L.-L. Feng 2021; J.-f. Mo et al. 2025). A statistically large sample of localized FRBs is thus crucial to improve signal-to-noise when comparing DMs of FRBs that intersect filaments to those that do not.

This paper probes the baryonic content of cosmic filaments using localized FRBs. Section 2 outlines the data and methodology used to detect baryons in filaments and estimate their baryon content; Section 3 presents the results; Section 5 summarizes our conclusions. Factors affecting the statistical significance are discussed in the Appendix. We adopt cosmological parameters: $\Omega_m = 0.3089$, $\Omega_b = 0.0486$, $\Omega_\Lambda = 0.6911$ and $h = 0.6774$ (Planck Collaboration et al. 2016).

2. METHODOLOGY

2.1. Galaxy catalog from DESI Legacy Imaging Surveys and filaments

H. Zou et al. (2019) published a catalog of photometric redshifts and stellar masses for ~ 300 million galaxies from the DESI Legacy Imaging Surveys (A. Dey et al. 2019), covering over $14,000 \text{ deg}^2$. The galaxies span redshifts up to $z \sim 1$ and stellar masses from $10^{8.4}$ to $10^{11.9} M_\odot$. The sky coverage is shown in blue in the top panel of Figure 1.

Using this galaxy catalog, we identify cosmic filaments using the DisPerSE algorithm³ (T. Sousbie 2011; T. Sousbie et al. 2011), which is widely applied to both observations (e.g., SDSS; N. Malavasi et al. 2020) and simulations (e.g., MillenniumTNG; D. Galárraga-Espinoza et al. 2024) in both two-dimensional (e.g., C. J. O’Kane et al. 2024) and three-dimensional (e.g., Y. M. Bahe & P. Jablonka 2025; Q.-R. Yang et al. 2025) analyses.

Given the photometric redshift uncertainty of ~ 0.02 in the DESI Legacy Imaging Surveys catalog (H. Zou et al. 2019), we divide the galaxy sample into 20 redshift bins of $\Delta z = 0.05$ across $0 < z < 1$. In each bin, cosmic filaments are identified in 2D using DisPerSE, based on the galaxies’ right ascension (RA) and declination (DEC). DisPerSE constructs the density field with the Delaunay Tessellation Field Estimator (DTFE; W. E. Schaap & R. van de Weygaert 2000; R. van de Weygaert & W. Schaap 2009) and extracts filamentary structures via discrete Morse theory by identifying critical points (minima, saddles, and maxima) in the gradient field.

³ <https://www2.iap.fr/users/sousbie/web/html/indexd41d.html?>

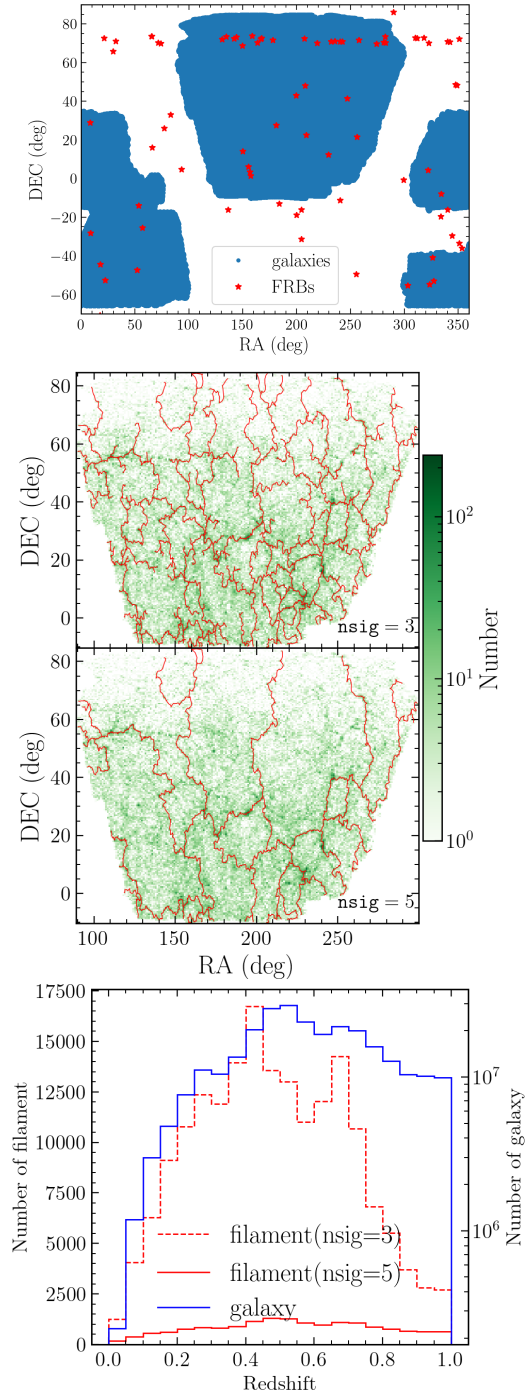


Figure 1. Top: The sky area (blue region) in the Dark Energy Spectroscopic Instrument (DESI) Legacy Imaging Surveys and positions of localized FRBs (red pentagrams). Middle: Filaments and galaxies at $z = 0-0.05$ across the northern sky. Red lines show filament skeletons identified by DisPerSE with $\text{nsig}=3$ and $\text{nsig}=5$ thresholds; green shading indicates galaxy density. Bottom: red lines show filament counts for $\text{nsig}=3$ (dashed) and $\text{nsig}=5$ (solid); blue line shows galaxy counts per redshift bin.

In DisPerSE, filaments are defined as pairs of field lines connecting saddle points to maxima. To filter out noise, DisPerSE applies persistence theory, which measures the topological significance of structures. Following N. Malavasi et al. (2020), we adopt persistence thresholds of $\text{nsig}=3$ and 5, corresponding to 3σ and 5σ significance levels. While $\text{nsig}=5$ yields more robust filaments, it may exclude weaker but real structures. We use $\text{nsig}=5$ as the default and compare with $\text{nsig}=3$ to assess threshold sensitivity. Further implementation details are provided in the Appendix A.

The middle panel of Figure 1 shows filament identification in the redshift range 0–0.05 across the northern sky, using persistence thresholds of $\text{nsig} = 3$ (top) and $\text{nsig} = 5$ (middle), overlaid on the galaxy distribution. The bottom panel displays the number of galaxies and filaments per redshift bin. Filament identification becomes incomplete beyond $z > 0.5$ due to the decreasing number of galaxies in the DESI imaging survey at higher redshifts.

2.2. Two groups of localized FRBs: intersected filaments or not

We use 84 localized FRBs, combining the 71 events compiled by J.-f. Mo et al. (2025) with 13 new ones—11 from the CRAFT survey (R. M. Shannon et al. 2025) and 2 from CHIME/FRB (X.-L. Chen et al. 2025; V. Shah et al. 2025). Their sky positions are shown as red pentagrams in the top panel of Figure 1. Of these, 46 lie within the DESI area. From this subset, we select 37 high-confidence FRBs (with $P_{\text{cc}} < 0.05$ or $P_{\text{host}} > 0.95$) to test whether their lines of sight intersect cosmic filaments. The 37 FRBs are divided into two groups: ‘Pass’, whose lines of sight intersect filaments from the galaxy catalog of DESI imaging surveys within redshift bins $j \cdot 0.05 < z < (j+1) \cdot 0.05$ ($j = 0, \dots, 19$), and ‘NoPass’, which do not intersect any filament. The filament redshift in each bin is approximated as $z_{\text{fila}}(j) \approx j \cdot 0.05 + 0.025$.

To identify filaments intersected by FRB sightlines, we estimate their angular width as $d = R_{\text{ini}}(1+z)/r_{\text{com}}$, where $R_{\text{ini}} = 2 \text{ Mpc}$ is the initial estimate of filament radius and r_{com} is the comoving distance to the filament’s redshift bin. The choice of $R_{\text{ini}} = 2 \text{ Mpc}$ is motivated by Q.-R. Yang et al. (2025), who find most filaments are less than 2 Mpc across. A filament is considered intersected if the FRB’s sky position falls within its projected angular width d and its redshift exceeds that of the filament. This selection method is illustrated in the upper panel of Figure 2.

To validate candidate filaments, we estimate their physical radius, R_{fila} , using the correlation with stel-

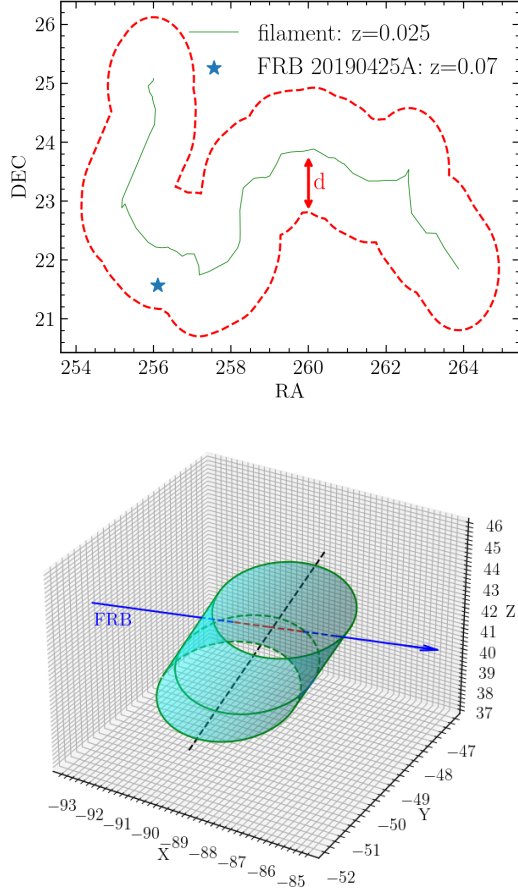


Figure 2. Upper: Example of an FRB intersecting a filament in 2D. The solid green line marks the filament spine, and ‘d’ indicates its angular width. Bottom: 3D illustration of an FRB-filament intersection. The black dashed line shows the filament’s skeleton, the cyan cylinder marks its region with radius R_{fila} , the blue line is the sightlines to FRB, and the red segment indicates the intersecting path.

lar mass per unit length from Q.-R. Yang et al. (2025), then check if the FRB line of sight intersects the filament’s cylindrical region of radius R_{fila} in 3D space (see lower panel of Figure 2). More details are provided in the Appendix B. FRBs meeting this criterion form the ‘Pass’ subgroup. Among 37 securely localized FRBs, we find 7 intersect filaments in our default catalog, totaling 12 crossings. Table 1 lists their classifications, number of intersections, and filament redshifts. We also determine the specific intersection paths (e.g., red segment in the bottom panel of Figure 2) used to model DM_{fila} , the dispersion measure from baryonic gas in filaments, as described below.

2.3. Modeling of DM caused by baryons in intersecting filaments

The DM in the rest frame is defined as the integral of the free electron number density n_e along the L.O.S., i.e.,

$$\text{DM} = \int n_e dl. \quad (1)$$

For those FRBs whose sightlines intersect cosmic filaments, we estimate the DM caused by filaments using the gas density profile modeled as an isothermal single β model with $\beta = 2/3$, following W. Zhu et al. (2021), i.e.,

$$\rho_{\text{gas}}(r) = \frac{\rho_{\text{gas},0}}{(1 + (\frac{r}{r_c})^2)^{\frac{3}{2}\beta}} = \frac{\rho_{\text{gas},0}}{1 + (\frac{r}{r_c})^2}, \quad (2)$$

where the core radius is set to $r_c = 0.64 R_{\text{fila}}$, and the central gas density is $\rho_{\text{gas},0} = (1 + \delta_0) \Omega_b \rho_{\text{crit}} (1 + z)^3$, where δ_0 is the central overdensity, Ω_b is the baryon density at $z = 0$, and $\rho_{\text{crit}} = 3H_0^2/(8\pi G)$ is the critical density; H_0 is the Hubble constant at $z = 0$, G is the Newtonian gravitational constant. According to Q.-R. Yang et al. (2025), we assume δ_0 is redshift-independent.

Considering a hydrogen (H) mass fraction of $Y_{\text{H}} = \frac{3}{4}$ and a helium (He) mass fraction of $Y_{\text{He}} = \frac{1}{4}$, along with ionization fractions $\chi_{\text{H}} \sim \chi_{\text{He}} \sim 1$ for filaments at redshift $z < 3$ (W. Deng & B. Zhang 2014), the resulting free electron number density in the filament is given by:

$$\begin{aligned} n_e(r) &= n_{\text{H}} \cdot Y_{\text{H}} \cdot \chi_{\text{H}} + 2n_{\text{He}} \cdot Y_{\text{He}} \cdot \chi_{\text{He}} \\ &= \frac{\rho_{\text{gas}}(r)}{m_p} \cdot Y_{\text{H}} \cdot \chi_{\text{H}} + 2 \frac{\rho_{\text{gas}}(r)}{4m_p} \cdot Y_{\text{He}} \cdot \chi_{\text{He}} \\ &= \frac{\rho_{\text{gas}}(r)}{m_p} \left(\frac{3}{4} + \frac{1}{2} \times \frac{1}{4} \right) = \frac{7}{8} \frac{\rho_{\text{gas}}(r)}{m_p}, \end{aligned} \quad (3)$$

where m_p is the mass of proton.

The DM contributed by an intersecting filament, DM_{fila} , is computed using Equation 1, with the integration path defined as in the previous section (see red line in the bottom panel of Figure 2).

2.4. Estimation of baryon mass in filaments

The observed DM of FRBs is the sum of multiple components:

$$\begin{aligned} \text{DM}_{\text{obs}} &= \text{DM}_{\text{MW,ISM}} + \text{DM}_{\text{MW,halo}} + \text{DM}_{\text{IGM}} \\ &\quad + \frac{\text{DM}_{\text{host}}}{1 + z_h} + \frac{\text{DM}_{\text{ForeH}}}{1 + z_{fh}}, \end{aligned} \quad (4)$$

where the subscripts ‘MW,ISM’, ‘MW,halo’, ‘IGM’, ‘Host’, ‘ForeH’ refer to the Milky Way’s interstellar medium, Milky Way halo, intergalactic medium, the host galaxy and its halo, and foreground galaxy halos, respectively. The redshifts of the host and foreground

Table 1. The basic information of 37 securely localized FRBs and derived results of FRB-intersected filaments.

Basic information of FRBs							Derived results of intersected filaments			
FRB	RA	DEC	redshift	DM _{obs}	P _{cc} /P _{host}	Ref.	Number	z _{fila}	DM _{fila}	
	degree	degree		pc cm ⁻³					pc cm ⁻³	
'Pass'	190425A	256.11	21.57	0.0715	127.8	0.0012/-	M. Bhardwaj et al. (2023)	1	0.025	27
	200906A	53.50	-14.08	0.3688	577.8	-/1	S. Bhandari et al. (2022)	2	0.175,0.225	73
	220105A	208.80	22.47	0.2784	583.0	-/1	A. C. Gordon et al. (2023)	2	0.025,0.075	56
	220509G	282.67	70.24	0.0894	269.5	-/0.99	C. J. Law et al. (2023)	1	0.025	32
	221219A	257.63	71.63	0.553	706.7	-/0.99	K. Sharma et al. (2024)	3	0.025,0.125,0.175	103
	230307A	177.78	71.70	0.2706	608.9	-/0.97	K. Sharma et al. (2024)	2	0.175,0.225	78
	240114A	321.92	4.33	0.1306	527.1	-/0.997	X.-L. Chen et al. (2025)	1	0.075	35
	180924B	326.10	-40.90	0.3214	361.4	0.0018/0.9994	K. E. Heintz et al. (2020)			
	181030A	158.58	73.75	0.0039	103.5	0.0025/-	M. Bhardwaj et al. (2021a)			
	181112A	327.35	-52.97	0.4755	589.3	0.0257/0.9274	J. X. Prochaska et al. (2019)			
	181223C	181.08	27.58	0.0302	111.6	0.04/-	M. Bhardwaj et al. (2023)			
	190608B	334.02	-7.90	0.1178	338.7	0.0016/1	S. Bhandari et al. (2020)			
	191001A	323.35	-54.75	0.234	506.9	0.0031/0.9995	K. E. Heintz et al. (2020)			
	200120E	149.49	68.83	-0.0001	87.8	0.0006/-	M. Bhardwaj et al. (2021b)			
200223B	8.27	28.83	0.06024	203.8	0.01/0.899	A. L. Ibik et al. (2023)				
200430A	229.71	12.38	0.16	380.1	0.0051/1.0	K. E. Heintz et al. (2020)				
210117A	339.98	-16.15	0.214	730.0	-/0.9984	S. Bhandari et al. (2023)				
211212A	157.35	1.36	0.0707	206.0	-/0.998	C. W. James et al. (2022)				
220204A	274.22	69.72	0.4012	612.584	-/0.99	K. Sharma et al. (2024)				
220310F	134.72	73.49	0.47796	462.24	-/0.99	C. J. Law et al. (2023)				
220418A	219.10	70.10	0.622	623.25	-/0.97	C. J. Law et al. (2023)				
220914A	282.06	73.34	0.1139	631.28	-/0.97	C. J. Law et al. (2023)				
220920A	240.26	70.92	0.15824	314.99	-/0.98	C. J. Law et al. (2023)				
221012A	280.80	70.52	0.28467	441.08	-/1.0	C. J. Law et al. (2023)				
221106A	56.70	-25.57	0.2044	343.8	-/0.9708	R. M. Shannon et al. (2025)				
230124	231.92	70.97	0.0939	590.574	-/0.99	K. Sharma et al. (2024)				
230526A	22.23	-52.72	0.157	361.4	-/0.997	R. M. Shannon et al. (2025)				
230626A	235.63	71.13	0.327	452.723	-/0.99	K. Sharma et al. (2024)				
230628A	166.79	72.28	0.127	344.952	-/0.95	K. Sharma et al. (2024)				
230708A	303.12	-55.36	0.105	411.51	-/1.0	R. M. Shannon et al. (2025)				
230712A	167.36	72.56	0.4525	587.567	-/0.99	K. Sharma et al. (2024)				
230902A	52.14	-47.33	0.3619	440.1	-/1.0	R. M. Shannon et al. (2025)				
231226A	155.36	6.11	0.1569	329.9	-/1.0	R. M. Shannon et al. (2025)				
240201A	149.91	14.09	0.042729	374.5	-/1.0	R. M. Shannon et al. (2025)				
240210A	8.78	-28.27	0.023686	283.73	-/1.0	R. M. Shannon et al. (2025)				
240310A	17.62	-44.44	0.127	601.8	-/0.9884	R. M. Shannon et al. (2025)				
'NoPass'										

halos are denoted by z_h and z_{fh} . The $(1+z)^{-1}$ factors account for the scaling relations between DM and frequency ν , along with time dilation and redshift resulting from cosmic expansion (K. Ioka 2003). The observed total DM and redshift distribution for the 37 well-localized FRBs are shown in the top-left panel of Figure 3.

DM_{IGM} includes contributions from diffuse gas outside halos—voids, walls, and filaments—with the filamentary part denoted as DM_{fila} . FRBs in the ‘Pass’ group, which intersect filaments, are expected to have systematically higher DM_{IGM} than those in the ‘NoPass’ group, especially at higher redshifts where more filaments are crossed. We estimate DM_{fila} from the offset between the $\text{DM}_{\text{IGM}}-z$ relations of the two groups. DM_{IGM} is obtained by subtracting contributions from the Milky Way (ISM and halo), the host galaxy (and its halo), and foreground halos from the total observed DM.

We estimate $\text{DM}_{\text{MW,ISM}}$ using the NE2001 model (J. M. Cordes & T. J. W. Lazio 2002), though the YMW16 model (J. M. Yao et al. 2017) is an alternative. The top right panel of Figure 3 shows the DMs of the 37 localized FRBs after subtracting $\text{DM}_{\text{MW,ISM}}$. $\text{DM}_{\text{MW,halo}}$ is assumed to be a constant $\sim 38 \text{ pc cm}^{-3}$, based on S. Yamasaki & T. Totani (2020) with a 68% confidence range of 32–45 pc cm^{-3} . As this value is applied uniformly, it does not affect the relative $\text{DM}_{\text{IGM}}-z$ differences between the Pass and NoPass groups.

For the host galaxy contribution, DM_{host} , we adopt a log-normal distribution with median $e_{\text{host}}^{\mu} = 130 \text{ pc cm}^{-3}$ and shape parameter $\sigma_{\text{host}} = 0.56$, following L. Connor et al. (2025), which based on a sample of 69 localized FRBs. Following G. Q. Zhang et al. (2020), we assume redshift evolution as $\text{DM}_{\text{host}} = 130(1+z_h) \text{ pc cm}^{-3}$. For comparison, J.-F. Mo et al. (2023) suggested a weaker evolution, $\text{DM}_{\text{host}} \propto (1+z_h)^{0.6}$, assuming FRBs trace the cosmic star formation rate. The uncertainty, $\sigma_{\text{DM}_{\text{host}}}$, is estimated from the median–16th percentile difference, yielding $\sim 60 \text{ pc cm}^{-3}$, which dominates the DM_{IGM} error at $z < 1$. We propagate this and adopt $\sigma_{\text{DM}_{\text{IGM}}} \approx 60 \text{ pc cm}^{-3}$. The impact of a larger $\sigma_{\text{DM}_{\text{host}}}$ is explored in the fourth paragraph of Appendix C. A larger $\sigma_{\text{DM}_{\text{host}}}$, which corresponds to a larger $\sigma_{\text{DM}_{\text{IGM}}}$, tends to alleviate the tensions in the $\text{DM}_{\text{IGM}}-z$ relation between the ‘Pass’ and ‘NoPass’ groups, as shown in Table 2.

To estimate the DM from intervening foreground halos, DM_{ForeH} , we identify candidate halos from the DESI group catalog (X. Yang et al. 2021). A halo contributes if the FRB’s L.O.S. intersects its r_{180} region and no filament intersects the same L.O.S. within the halo’s redshift bin or its two adjacent bins—this avoids double-counting due to photometric redshift uncertainties and

group–filament associations. For qualifying halos, we compute DM_{ForeH} following Y. Huang et al. (2025). We assume halos with $M_{\text{halo}} < 10^{13.5} M_{\odot}$ follow a modified NFW (mNFW) gas profile (J. X. Prochaska & Y. Zheng 2019):

$$\rho_b(r) = f_{\text{gas}} \frac{\rho_0(M_{\text{halo}})}{y^{1-\alpha}(y_0 + y)^{2+\alpha}} \quad (5)$$

where $\rho_0(M_{\text{halo}})$ denotes the central gas density as a function of halo mass; $y \equiv c(r/R_{\text{vir}})$ with c being the concentration parameter; Following Y. Huang et al. (2025), we fix y_0 and α to 2. The hot gas fraction, f_{gas} , is calibrated using R_{200} -based scaling relations from P. Popesso et al. (2024):

$$f_{\text{gas}} = 2.09 \times 10^{-6} (M_{200}/M_{\odot}), \quad (6)$$

where M_{200} is mass within R_{200} . For halos with $M_{\text{halo}} > 10^{13.5} M_{\odot}$, we adopt the ICM model from A. Vikhlinin et al. (2006), updating the gas fraction using the same equation above. In both the mNFW (group-scale) and ICM (cluster-scale) models, the gas profile is truncated at $r_{\text{max}} = R_{\text{vir}}$. DM_{ForeH} is computed by integrating the gas density along the FRB sightline using the `Ne_Rperp` routine from J. X. Prochaska et al. (2025).

After subtracting contributions from the Milky Way, host galaxy and CGM, and foreground halos, we obtain DM_{IGM} and its uncertainty $\sigma_{\text{DM}_{\text{IGM}}}$ for FRBs in both ‘Pass’ and ‘NoPass’ groups. We then estimate the baryonic mass in filaments by analyzing the difference in their $\text{DM}_{\text{IGM}}-z$ relations. The procedure is detailed below.

We first fit a linear function, $f_{\text{NoPass}}(z)$, to the $\text{DM}_{\text{IGM}}-z$ relation for the ‘NoPass’ subgroup, following J. M. Cordes et al. (2022) and J.-f. Mo et al. (2025), who find this relation can be approximated as linear. For FRBs in ‘Pass’ group, we assume a constant filament baryon central overdensity δ_0 (10–100) and estimate DM_{fila} using the method in Section 2.3. The DM caused by the diffuse IGM in voids and walls, i.e., excluding filament contributions, is then $\text{DM}_{\text{IGM,Pass-corr}} = \text{DM}_{\text{IGM,Pass}} - \text{DM}_{\text{fila}}$.

We use the Python package `emcee` (D. Foreman-Mackey et al. 2013) to run Markov Chain Monte Carlo (MCMC) simulations and infer the optimal filament central overdensity δ_0 by minimizing the difference between the corrected $\text{DM}_{\text{IGM,Pass-corr}}-z$ relation and the linear fit $f_{\text{NoPass}}(z)$. The adopted log-likelihood function is:

$$\begin{aligned} \log \mathcal{L} = & -\frac{1}{2} \sum_i^{N_{\text{FRB,Pass}}} \left(\frac{(\text{DM}_{\text{IGM,Pass-corr},i} - f_{\text{NoPass}}(z_i))^2}{\sigma_i^2} \right. \\ & \left. + \log(2\pi\sigma_i^2) \right), \end{aligned} \quad (7)$$

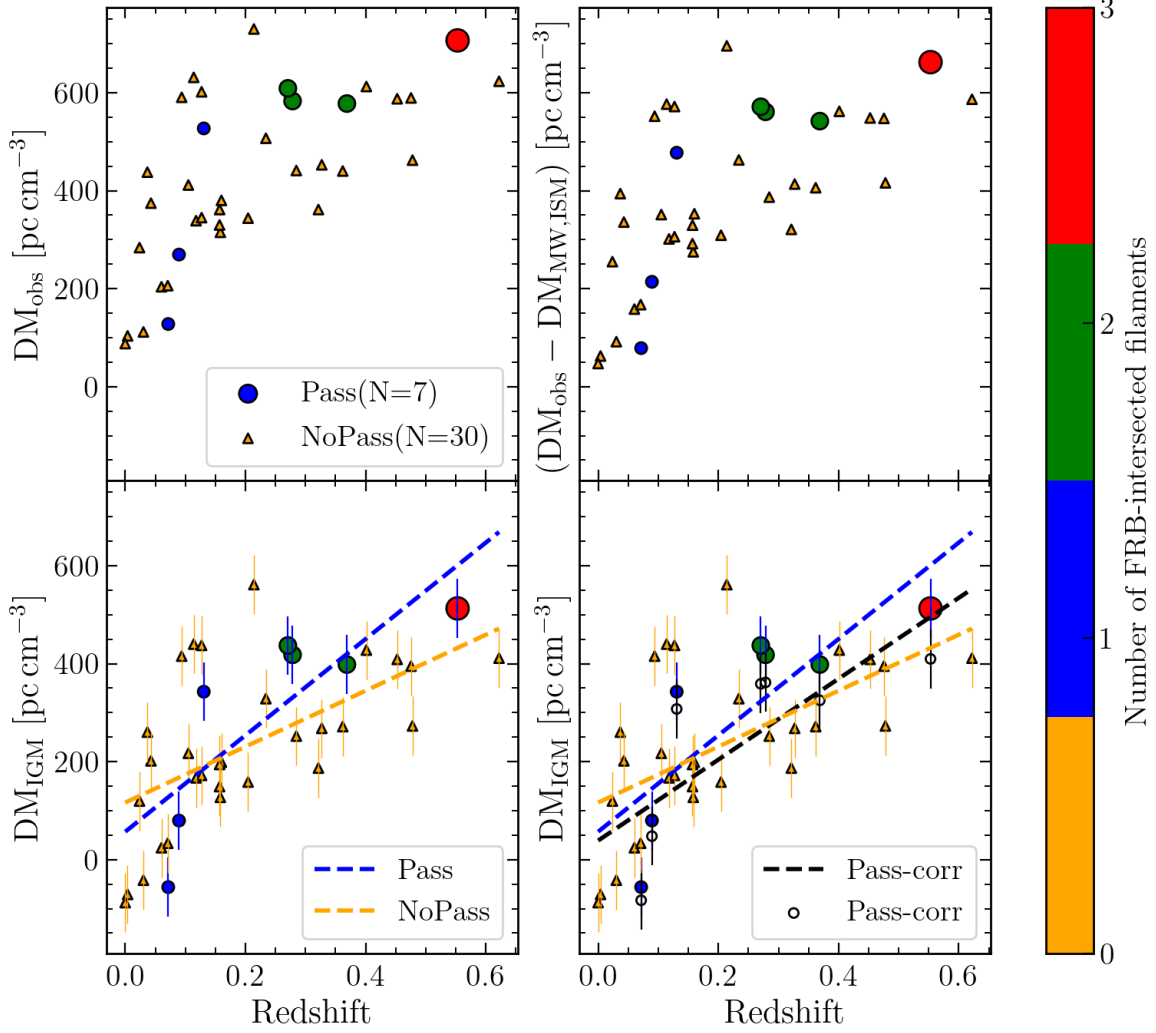


Figure 3. Top: Distributions of DM_{obs} (left) and $DM_{\text{obs}} - DM_{\text{MW,ISM}}$ (right) and redshifts for 37 well-localized FRBs in the DESI area, divided into ‘Pass’ (circles) and ‘NoPass’ (yellow triangles) groups. Circle color and size indicate the number of intersected filaments. Bottom Left: DM_{IGM} vs. redshift for the same FRBs. Dashed lines show best-fit linear trends for each group; error bars represent uncertainties of $\sim 60 \text{ pc cm}^{-3}$. Bottom Right: Same as left, but with filament contributions subtracted: $DM_{\text{IGM,Pass-corr}} = DM_{\text{IGM,Pass}} - DM_{\text{fila}}$ (open circles), using central gas overdensity in filaments $\delta_0 = 20.78$. The black dashed line shows the corresponding linear fit.

where $\sigma_i^2 = \sigma_{\text{Pass},i}^2 + \sigma_{\text{NoPass},i}^2$, with $\sigma_{\text{Pass},i}^2$ representing the uncertainty in DM_{IGM} for the i -th FRB in the ‘Pass’ group at redshift z_i , and $\sigma_{\text{NoPass},i}^2$ denoting the fitting error of the linear function f_{NoPass} at z_i .

With the optimal central overdensity δ_0 determined, the total gas mass in a filament is calculated as:

$$M_{\text{gas,fil},i} = \int_0^{L_{\text{fila}}} dl \int_0^{R_{\text{fila}}} 2\pi r \rho_{\text{gas}}(r) dr, \quad (8)$$

where L_{fila} is the filament length, R_{fila} its radius, and $\rho_{\text{gas}}(r)$ the radial gas density profile.

The gas mass density from filaments in the j -th redshift bin is calculated by summing the gas masses of all identified filaments in that bin and dividing by the

corresponding comoving volume:

$$\rho_{\text{gas,fil},j} = \frac{\sum_{i=1}^{N_{\text{fila},j}} M_{\text{gas,fil},i}}{V_c \cdot f_{\text{DESI}}}, \quad (9)$$

where $N_{\text{fila},j}$ is the number of filaments in the bin, V_c is the comoving volume between redshifts $j \cdot 0.05$ and $(j+1) \cdot 0.05$, and $f_{\text{DESI}} \approx 0.44$ is the DESI sky area fraction (X. Yang et al. 2021).

For each redshift bin, the baryon fraction in filaments is $\Omega_{b,\text{fil},j} = \rho_{\text{gas,fil},j} / \rho_{\text{crit},j}$, where $\rho_{\text{crit},j}$ is the critical density at the bin’s median redshift. The average value for $z < 1$ is denoted as $\bar{\Omega}_{b,\text{fil}}$.

3. RESULTS

3.1. $\text{DM}_{\text{IGM}}-z$ relationships of two FRB groups

Among 37 securely localized FRBs in the DESI area, 7 intersect filaments identified by DisPerSE using galaxies with $M_* > 10^9 M_\odot$ and $\text{nsig}=5$, while 30 do not (see Figure 3). We quantify the difference by fitting separate linear regressions to the $\text{DM}_{\text{IGM}}-z$ relations for the ‘Pass’ and ‘NoPass’ groups. The best-fit relations are:

$$\text{DM}_{\text{IGM,Pass}} = a_1 z + b_1 = (982 \pm 136) \cdot z + (58 \pm 40), \quad (10)$$

$$\text{DM}_{\text{IGM,NoPass}} = a_2 z + b_2 = (573 \pm 65) \cdot z + (116 \pm 16). \quad (11)$$

The parameter covariance matrices are $\text{cov}_1 = \begin{pmatrix} 18461 & -4656 \\ -4656 & 1644 \end{pmatrix}$ and $\text{cov}_2 = \begin{pmatrix} 4229 & -838 \\ -838 & 276 \end{pmatrix}$. The difference between the fit parameters is given by $\mathbf{D} = (a_1 - a_2, b_1 - b_2)$, and the chi-square statistic is $\chi^2 = \mathbf{D}(\text{cov}_1 + \text{cov}_2)^{-1} \mathbf{D}^T = 10.29$, yielding a p-value of 0.006, or $\sim 2.8\sigma$, assuming a chi-square distribution with 2 degrees of freedom. This result indicates a statistically significant 2.8σ difference in the $\text{DM}_{\text{IGM}}-z$ relation between the ‘Pass’ and ‘NoPass’ groups.

J. M. Cordes et al. (2022) found $\text{DM}_{\text{IGM}} \approx 826z \text{ pc cm}^{-3}$ assuming a constant IGM fraction $f_{\text{IGM}} = 0.85$, while J.-f. Mo et al. (2025) reported $\text{DM}_{\text{IGM}} = 861z - 25 \text{ pc cm}^{-3}$ using a redshift-dependent $f_{\text{IGM}}(z)$ from TNG100. These values fall between our ‘Pass’ and ‘NoPass’ results—higher than the latter and lower than the former—as expected, since they reflect the average IGM contribution, including diffuse gas in voids, walls, and filaments.

As shown in the bottom left panel of Figure 3, the $\text{DM}_{\text{IGM}}-z$ relations for the ‘Pass’ and ‘NoPass’ groups diverge at higher redshifts, as distant FRBs are more likely to intersect filaments, increasing their DM. This difference becomes more significant with larger samples—reaching 4.9σ with all 46 FRBs in the DESI area, and up to 5.9σ when considering only those at $z > 0.1$. Using a lower persistence threshold ($\text{nsig}=3$) reduces the significance to 2.4σ (37 FRBs) and 3.5σ (46 FRBs). Details on the factors affecting this significance, including number of localized FRBs, the redshift range of selected samples, the assumed $\sigma_{\text{DM}_{\text{host}}}$, and filaments classification procedure are provided in Appendix C.

3.2. Baryon mass in filaments

Using the method in Section 2.4, we perform MCMC sampling with 10 walkers, 500 burn-in steps, and 5000 total steps to estimate the optimal central baryon overdensity in filaments. Convergence, typically achieved when the chain length exceeds $50\tau_f$ (D. Foreman-

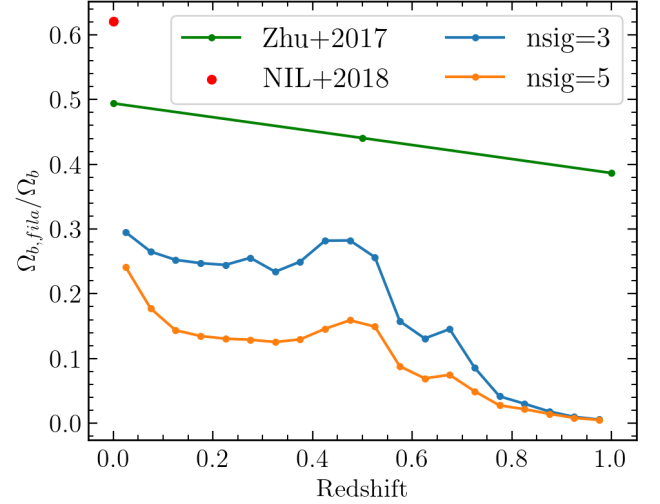


Figure 4. Estimated baryon mass fraction in filaments across redshift bins. Blue and orange lines show results from this work using 37 securely localized FRBs within DESI area and DisPerSE-identified filaments (galaxy catalog from DESI imaging surveys) with persistence thresholds $\text{nsig}=3$ and $\text{nsig}=5$, respectively. The green line and red point represent estimates from simulations by W. Zhu & L.-L. Feng (2017) and N. I. Libeskind et al. (2018).

Mackey et al. 2013), was reached after ~ 4000 steps in our case.

The MCMC analysis yields an optimal central overdensity of $\delta_0 = 21^{+13}_{-12}$, assuming an isothermal single- β model with $\beta = 2/3$. The corrected DM_{IGM} , $\text{DM}_{\text{IGM,Pass-corr}} = \text{DM}_{\text{IGM,Pass}} - \text{DM}_{\text{fila}}$, are shown in the bottom right panel of Figure 3, with DM_{fila} values listed in Table 1. On average, each intersected filament contributes about 34 pc cm^{-3} .

This best-fit central overdensity is broadly consistent with predictions from hydrodynamical simulations (e.g., W. Zhu & L.-L. Feng 2017; D. Martizzi et al. 2019; T. Tuominen et al. 2021; W. Zhu et al. 2021; D. Galárraga-Espinosa et al. 2022; Q.-R. Yang et al. 2025) and aligns well with several observational estimates. It agrees with $\delta_0 \sim 19$ from tSZ measurements of filaments identified in SDSS DR12 (H. Tanimura et al. 2020a) and $\delta_0 \sim 21$ from X-ray emission measurements of filaments using SRG/eROSITA (H. Tanimura et al. 2022), but is higher than the $\delta_0 \sim 3.2\text{--}5.5$ values reported by H. Tanimura et al. (2019) and A. de Graaff et al. (2019) based on tSZ measurements of filaments between galaxy group pairs.

Using Equations 8 and 9, we derive the baryon mass fraction in filaments for each redshift bin, shown in Figure 4. With $\text{nsig}=5$ in filament identification, the fraction declines from $0.25\Omega_b$ at $z = 0.02$ to $0.15\Omega_b$ at $z = 0.5$, and $0.03\Omega_b$ at $z = 0.8$. Lowering the threshold to $\text{nsig}=3$ raises these to 0.30 , 0.30 , and 0.04 , re-

spectively. The bump in $\Omega_{b,\text{fila}}$ between $z = 0.4$ and 0.55 is due to a higher filament count in that range (Figure 1). Averaged over $z < 1$, filaments contribute $\Omega_{b,\text{fila}} = 0.10\Omega_b$ for `nsig=5` and $0.17\Omega_b$ for `nsig=3`.

Our measurement agrees with the tSZ-based estimate from H. Tanimura et al. (2020a), who found $\Omega_{b,\text{fila}} = 0.08\Omega_b$ for SDSS filaments at $0.2 < z < 0.6$. More recently, Li et al. (submitted) used Planck Compton- y and CMB lensing maps to estimate $\Omega_{b,\text{fila}} = 0.12^{+0.020}_{-0.021}\Omega_b$ at $0.2 < z < 0.6$ for long filaments ($30\text{--}100 h^{-1} \text{ Mpc}$) identified from SDSS DR12, and $0.227^{+0.036}_{-0.035}\Omega_b$ for filaments of all lengths.

Even with `nsig=3`, the derived filament baryon fractions at $z < 1$ are still below the 30%–60% predicted by simulations (e.g., W. Zhu & L.-L. Feng 2017; N. I. Libeskind et al. 2018). This discrepancy likely stems from the incompleteness of our filament sample, limited by the galaxy density in the DESI imaging catalog—especially at $z > 0.5$, where many filaments may be missed.

4. SUMMARY

We classify fast radio bursts (FRBs) into two groups based on whether their lines of sight intersect cosmic filaments (‘Pass’) or not (‘NoPass’), with filaments identified using the DisPerSE algorithm applied to galaxies with $M_* > 10^9 M_\odot$ from DESI imaging surveys. We find tentative ($\sim 3\sigma$) evidence for a divergence in the $\text{DM}_{\text{IGM}}\text{--}z$ relation between the two groups. Assuming this divergence arises from ionized baryons in filaments and modeling their gas with an isothermal β -profile ($\beta = 2/3$), MCMC analysis yields a central baryon overdensity of $\delta = 21^{+13}_{-12}$.

The inferred central overdensity broadly aligns with both hydrodynamical simulations and observational estimates from tSZ and X-ray data. Using this value, we estimate that filaments host $\Omega_{b,\text{fila}} = 0.10\text{--}0.17\Omega_b$ at $z < 1$. The fraction declines from $0.25\text{--}0.30\Omega_b$ at $z = 0.02$ to $0.15\text{--}0.30\Omega_b$ at $z = 0.5$, and $0.03\text{--}0.04\Omega_b$ at $z = 0.8$. These values likely represent lower limits due to catalog incompleteness, especially at $z > 0.5$.

This study offers an independent method to trace baryons in cosmic filaments and refine their density estimates, contributing to resolving the missing baryon problem. Our findings underscore the need for larger samples of localized FRBs and galaxies, along with com-

plementary probes like X-ray emission and the Sunyaev-Zel’dovich effect, for further validation and improvement.

We performed a simplified random modeling analysis and found that approximately 90–100 high-confidence localized FRBs are needed to reach a 5σ tension in the $\text{DM}_{\text{IGM}}\text{--}z$ relation between the ‘Pass’ and ‘NoPass’ groups, if $\sigma_{\text{DM}_{\text{IGM}}} = 100 \text{ pc cm}^{-3}$, which is more conservative than the 60 pc cm^{-3} adopted in our default model. We generate mock FRBs with redshifts drawn from the distribution of all localized FRBs in the DESI region. A Pass-to-NoPass ratio of 1:4 was adopted for mock events, which is similar to the observed ratio of 7:30 among the 37 securely localized FRBs. Their DM_{IGM} values were assigned by sampling from log-normal distributions with variance $\sigma_{\text{DM}_{\text{IGM}}}^2$ and mean values determined by the corresponding fitted $\text{DM}_{\text{IGM}}\text{--}z$ relations derived from these 37 FRBs under $\sigma_{\text{DM}_{\text{IGM}}} = 100 \text{ pc cm}^{-3}$.

ACKNOWLEDGMENTS

We thank the anonymous referee for his/her valuable suggestions, which have helped improve the manuscript. We thank Zhi-Qi Huang for his helpful discussion. This work is supported by the National Natural Science Foundation of China (NSFC) through grant 11733010, 12173102, and 12203107, and by the China Manned Space Program through its Space Application System.. This work has used the HPC facility of the School of Physics and Astronomy, Sun Yat-Sen University.

AUTHOR CONTRIBUTIONS

WSZ conceived the initial research concept and was responsible for writing and submitting the manuscript. JFM conducted the formal analysis and validation and also contributed to the initial draft. QRY, YZ, and LLF contributed to both the analysis and the development of the research concept.

Software: DisPerSE (T. Sousbie 2011; T. Sousbie et al. 2011)

APPENDIX

A. FILAMENT CLASSIFICATION

The details for how we identify filaments from the galaxy catalog in DESI imaging survey using DisPerSE algorithm are as follows. We first compute the 2D density field of the galaxy distribution using the `delaunay_2D` function in DisPerSE, which implements the Delaunay Tessellation Field Estimator (DTFE; W. E. Schaap & R. van de Weygaert 2000; R. van de Weygaert & W. Schaap 2009). We select galaxies with stellar masses $M_* > 10^9 M_\odot$, a mass cut consistent with a number of previous studies (e.g. D. Galárraga-Espinosa et al. 2024; C. J. O’Kane et al. 2024; Q.-R. Yang et al. 2025). To deal with boundary conditions in the observational sample area, D. J. Cornwell et al. (2022) generated a random uniform distribution of artificial galaxies beyond the boundary. Similarly, we utilize the `-btype smooth` parameter in the `delaunay_2D` function, consistent with N. Malavasi et al. (2020). This approach adds supplementary particles outside the boundary by interpolating the estimated density within boundary.

Next, we smooth the density field one time using the `netconv` function, which averages the density values with those of their direct neighbors in the network. Subsequently, we extract filaments from the smoothed galaxy density field using the `mse` function, which implements discrete Morse theory. This involves computing the gradients of the density field and identifying critical points (minima, saddles, and maxima) where the gradient vanishes. A filament is defined by the `skelconv` function as two field lines originating from a saddle point and connecting two maxima. The resulting filament skeleton remains unsmoothed in this work.

Spurious filaments, likely arising from Poisson noise in the discrete galaxy distribution, are eliminated using persistence theory within DisPerSE. Following N. Malavasi et al. (2020), we set the `nsig` parameter in the `mse` function to 3 or 5. This means structures with a probability less than 3σ or 5σ of appearing in a random field are removed. Consequently, filaments extracted with a higher persistence threshold are more robust than those extracted with a lower threshold, but may lose real weak filaments. With due caution, we adopt results with a 5σ (`nsig=5`) persistence threshold as our default sample of filaments, which will be compared with results with `nsig=3` to inspect the impact.

As an example, the middle panel in Figure 1 show filaments identified within redshift range 0 – 0.05 using a `nsig=3` and `nsig=5`, respectively, alongside the galaxy distribution. The bottom panel in Figure 1 shows the numbers of galaxies and filaments we identified in each redshift bin.

B. PROCEDURES OF IDENTIFYING INTERSECTED FILAMENTS

After finding candidate intersected filaments, we estimate their physical radius, R_{fila} , based on the correlation between the R_{fila} and the stellar mass per unit length contained within the filament found by Q.-R. Yang et al. (2025). Based on the Illustris-TNG simulation, Q.-R. Yang et al. (2025) find that R_{fila} correlates with the stellar mass per unit length contained within the filament, denoted as M_*/L_{fila} . In this context, R_{fila} is defined as the radial distance from the filament spine at which the gas density drops to the mean cosmic baryon density. The relationship between R_{fila} and M_*/L_{fila} is provided by fitting results at redshifts 0, 0.5, 1.0, and 2.0 as follows:

$$\begin{aligned} \log_{10}(R_{\text{fila}}) &= \frac{\log_{10}(M_*/L_{\text{fila}}) + 1.58}{2.535}, z = 0 \\ \log_{10}(R_{\text{fila}}) &= \frac{\log_{10}(M_*/L_{\text{fila}}) + 0.285}{2.233}, z = 0.5 \\ \log_{10}(R_{\text{fila}}) &= \frac{\log_{10}(M_*/L_{\text{fila}}) + 0.26}{2.364}, z = 1 \\ \log_{10}(R_{\text{fila}}) &= \frac{\log_{10}(M_*/L_{\text{fila}}) - 3.209}{1.412}, z = 2 \end{aligned} \tag{B1}$$

where L_{fila} is the filament length in comoving kiloparsecs (ckpc), while R_{fila} and M_* are given in ckpc and solar masses (M_\odot), respectively. To estimate R_{fila} at arbitrary redshifts, we apply linear interpolation between the fitting relations at $z = 0, 0.5, 1.0$, and 2.0 .

Using the filament skeleton determined by DisPerSE as the central axis, we calculate the total stellar mass within a cylindrical volume of initial radius 2 Mpc from the galaxy catalog. From this, we obtain an initial estimate of the filament radius via Equation B1. This radius is then iteratively refined by repeating the procedure: updating the cylindrical radius and recalculating the enclosed stellar mass. The iteration proceeds until the relative change in radius between steps falls below 5%, or a maximum of 10 iterations is reached. The final value is adopted as R_{fila} , with an

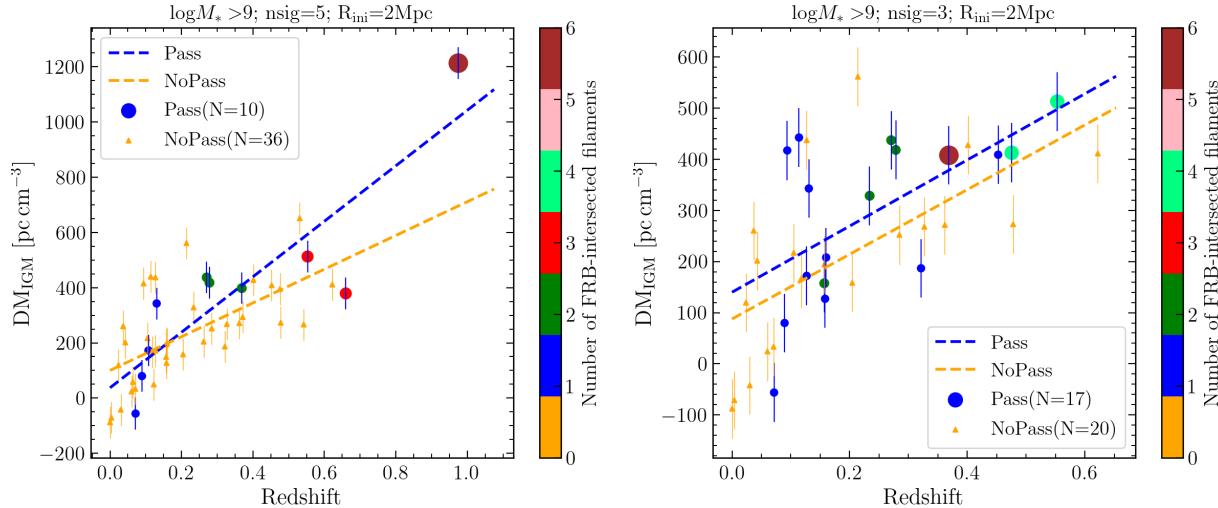


Figure 5. Similar to Figure 3, the left panel presents results based on all 46 localized FRBs within the DESI sky area, using filaments identified by DisPerSE with a persistence threshold of $\text{nsig}=5$. In contrast, the right panel shows results for the 37 securely localized FRBs, with filaments extracted using a lower threshold of $\text{nsig}=3$.

upper limit of 5 Mpc imposed to avoid overestimation. It is worth noting that limited galaxy sampling in the DESI imaging survey at high redshift may lead to underestimated filament radii.

With the improved estimation of filament widths, we then verify whether FRB line of sight (L.O.S.) intersects the candidate filaments in three-dimensional space, and subsequently compute the corresponding DM_{fila} . This process involves converting the FRB and filament positions from sky coordinates to Cartesian coordinates using the following transformation:

$$\begin{aligned} X &= r_{\text{com}} \cdot \cos(\text{RA}) \cdot \cos(\text{DEC}), \\ Y &= r_{\text{com}} \cdot \sin(\text{RA}) \cdot \cos(\text{DEC}), \\ Z &= r_{\text{com}} \cdot \sin(\text{DEC}). \end{aligned} \tag{B2}$$

An FRB is considered to intersect a filament if its line of sight passes through the filament's cylindrical region of radius R_{fila} in three-dimensional space. The intersection path is shown as the red segment in the bottom panel of Figure 2.

C. FACTORS MAY INFLUENCE THE STATISTICAL SIGNIFICANCE

Several factors may influence the statistical significance of our results, including the number and reliability of localized FRBs, the redshift distribution of the selected sample, the uncertainty in DM_{IGM} ($\sigma_{\text{DM}_{\text{IGM}}}$), the method used to classify filaments, and the assumed value of the initial filament radius R_{ini} . We examine these aspects below.

Increasing the number of well-localized FRBs is essential to enhance the robustness of our conclusions. As illustrated in the left column of Figure 5, when all localized FRBs within the DESI sky area ($N_{\text{FRB}} = 46$) are included, the difference in the $\text{DM}_{\text{IGM}}-z$ relations between the ‘Pass’ and ‘NoPass’ groups reaches a statistical significance of 4.9σ .

Focusing exclusively on localized FRBs at intermediate to high redshifts can improve the statistical significance of our results, as the relative contribution of the IGM to the total DM increases with redshift compared to nearby events. To evaluate this effect, we repeat our analysis using securely localized FRBs with $z > 0.1$ ($N_{\text{FRB}} = 26$) and $\text{nsig}=5$, while keeping all other procedures unchanged. This yields 3.7σ evidence for a divergent trend in the $\text{DM}_{\text{IGM}}-z$ relation between the ‘Pass’ and ‘NoPass’ groups. When applying the same analysis to the full sample of localized FRBs within the DESI sky coverage at $z > 0.1$ ($N_{\text{FRB}} = 34$), the statistical significance increases to 5.9σ . Therefore, the accumulation of additional localized FRBs at $z > 0.1$ in the future will be crucial for strengthening the statistical robustness of the $\text{DM}_{\text{IGM}}-z$ relations and further testing our findings.

Our default model adopts an uncertainty of $\sigma_{\text{DM}_{\text{IGM}}} \sim 60 \text{ pc cm}^{-3}$ (L. Connor et al. 2025), yielding a 2.8σ level of significance for the securely localized FRB sample ($N_{\text{FRB}} = 37$). Increasing $\sigma_{\text{DM}_{\text{IGM}}}$ to $\sim 100 \text{ pc cm}^{-3}$ reduces the significance to 1.3σ . Considering an even larger uncertainty based on the redshift-evolving DM_{host} model from TNG

simulations by J.-F. Mo et al. (2023), which suggests $\text{DM}_{\text{host}} \sim 170\text{--}220 \text{ pc cm}^{-3}$, the significance further decreases to 0.5σ . The relatively large uncertainty in DM_{host} arises from the diversity of host galaxy types among localized FRBs, including both star-forming and quiescent systems, as well as spiral and elliptical morphologies. However, the impact of this large $\sigma_{\text{DM}_{\text{host}}}$ —and consequently the uncertainty in $\sigma_{\text{DM}_{\text{IGM}}}$ —is expected to decline as the number of localized FRBs increases. For instance, applying the same analysis to all localized FRBs within the DESI sky coverage ($N_{\text{FRB}} = 46$) yields improved significance levels of 2.6σ and 1.4σ when adopting $\sigma_{\text{DM}_{\text{IGM}}} = 100$ and $170\text{--}200 \text{ pc cm}^{-3}$, respectively—demonstrating that a larger sample size can mitigate the effects of increased uncertainty in DM_{host} and DM_{IGM} .

We also evaluate the impact of using filaments extracted with a lower persistence threshold of `nsig=3`, compared to the default `nsig=5`, based on the 37 securely localized FRB samples and assuming $\sigma_{\text{DM}_{\text{IGM}}} \sim 60 \text{ pc cm}^{-3}$. This lower threshold increases the number of FRBs whose sightlines intersect filaments—including those deemed less significant—raising the count to 17, in contrast to 7 under the `nsig=5` setting (see the right panel of Figure 5). Under these conditions, the statistical significance of the difference in the $\text{DM}_{\text{IGM}}\text{--}z$ relation between the ‘Pass’ and ‘NoPass’ groups reaches 2.4σ . Furthermore, when the full set of 46 localized FRBs within the DESI sky coverage is used, the corresponding significance increases to 3.5σ .

The choice of input galaxy data influences the reconstructed density field and, consequently, the filament extraction. We test an alternative selection by using galaxies with stellar masses $M_* > 10^{10} M_{\odot}$ to identify filaments and find a statistical significance of 3.2σ for both `nsig=5` and `nsig=3` persistence thresholds. Additionally, we examine the impact of the adopted initial guess for the filament width, R_{ini} . When setting $R_{\text{ini}} = 5 \text{ Mpc}$, the significance of the difference between the ‘Pass’ and ‘NoPass’ groups drops to 1.4σ for the securely localized FRB sample ($N_{\text{FRB}} = 37$), and to 2.9σ for the full localized FRB sample within the DESI sky area ($N_{\text{FRB}} = 46$). A summary of all these tests is provided in Table 2.

REFERENCES

- Akamatsu, H., Fujita, Y., Akahori, T., et al. 2017, *A&A*, 606, A1, doi: [10.1051/0004-6361/201730497](https://doi.org/10.1051/0004-6361/201730497)
- Bahe, Y. M., & Jablonka, P. 2025, arXiv e-prints, arXiv:2502.06484, doi: [10.48550/arXiv.2502.06484](https://doi.org/10.48550/arXiv.2502.06484)
- Bhandari, S., Sadler, E. M., Prochaska, J. X., et al. 2020, *ApJL*, 895, L37, doi: [10.3847/2041-8213/ab672e](https://doi.org/10.3847/2041-8213/ab672e)
- Bhandari, S., Heintz, K. E., Aggarwal, K., et al. 2022, *AJ*, 163, 69, doi: [10.3847/1538-3881/ac3aec](https://doi.org/10.3847/1538-3881/ac3aec)
- Bhandari, S., Gordon, A. C., Scott, D. R., et al. 2023, *ApJ*, 948, 67, doi: [10.3847/1538-4357/acc178](https://doi.org/10.3847/1538-4357/acc178)
- Bhardwaj, M., Kirichenko, A. Y., Michilli, D., et al. 2021a, *ApJL*, 919, L24, doi: [10.3847/2041-8213/ac223b](https://doi.org/10.3847/2041-8213/ac223b)
- Bhardwaj, M., Gaensler, B. M., Kaspi, V. M., et al. 2021b, *ApJL*, 910, L18, doi: [10.3847/2041-8213/abeaa6](https://doi.org/10.3847/2041-8213/abeaa6)
- Bhardwaj, M., Michilli, D., Kirichenko, A. Y., et al. 2023, arXiv e-prints, arXiv:2310.10018, doi: [10.48550/arXiv.2310.10018](https://doi.org/10.48550/arXiv.2310.10018)
- Bonamente, M., Nevalainen, J., Tilton, E., et al. 2016, *MNRAS*, 457, 4236, doi: [10.1093/mnras/stw285](https://doi.org/10.1093/mnras/stw285)
- Bonjean, V., Aghanim, N., Salomé, P., Douspis, M., & Beelen, A. 2018, *A&A*, 609, A49, doi: [10.1051/0004-6361/201731699](https://doi.org/10.1051/0004-6361/201731699)
- Bregman, J. N., Otte, B., Irwin, J. A., et al. 2009, *ApJ*, 699, 1765, doi: [10.1088/0004-637X/699/2/1765](https://doi.org/10.1088/0004-637X/699/2/1765)
- Cen, R., & Ostriker, J. P. 1999, *ApJ*, 514, 1, doi: [10.1086/306949](https://doi.org/10.1086/306949)
- Chen, X.-L., Tsai, C.-W., Li, D., et al. 2025, *ApJL*, 980, L24, doi: [10.3847/2041-8213/adadfd](https://doi.org/10.3847/2041-8213/adadfd)
- CHIME/FRB Collaboration, Amiri, M., Andersen, B. C., et al. 2021, *ApJS*, 257, 59, doi: [10.3847/1538-4365/ac33ab](https://doi.org/10.3847/1538-4365/ac33ab)
- Connor, L., Ravi, V., Sharma, K., et al. 2025, *Nature Astronomy*, 9, 1226, doi: [10.1038/s41550-025-02566-y](https://doi.org/10.1038/s41550-025-02566-y)
- Cordes, J. M., & Chatterjee, S. 2019, *ARA&A*, 57, 417, doi: [10.1146/annurev-astro-091918-104501](https://doi.org/10.1146/annurev-astro-091918-104501)
- Cordes, J. M., & Lazio, T. J. W. 2002, arXiv e-prints, astro. <https://arxiv.org/abs/astro-ph/0207156>
- Cordes, J. M., Ocker, S. K., & Chatterjee, S. 2022, *ApJ*, 931, 88, doi: [10.3847/1538-4357/ac6873](https://doi.org/10.3847/1538-4357/ac6873)
- Cornwell, D. J., Kuchner, U., Aragón-Salamanca, A., et al. 2022, *MNRAS*, 517, 1678, doi: [10.1093/mnras/stac2777](https://doi.org/10.1093/mnras/stac2777)
- Cui, W., Knebe, A., Yepes, G., et al. 2018, *MNRAS*, 473, 68, doi: [10.1093/mnras/stx2323](https://doi.org/10.1093/mnras/stx2323)
- Danforth, C. W., Keeney, B. A., Tilton, E. M., et al. 2016, *ApJ*, 817, 111, doi: [10.3847/0004-637X/817/2/111](https://doi.org/10.3847/0004-637X/817/2/111)
- Davé, R., Cen, R., Ostriker, J. P., et al. 2001, *ApJ*, 552, 473, doi: [10.1086/320548](https://doi.org/10.1086/320548)
- de Graaff, A., Cai, Y.-C., Heymans, C., & Peacock, J. A. 2019, *A&A*, 624, A48, doi: [10.1051/0004-6361/201935159](https://doi.org/10.1051/0004-6361/201935159)
- Deng, W., & Zhang, B. 2014, *ApJL*, 783, L35, doi: [10.1088/2041-8205/783/2/L35](https://doi.org/10.1088/2041-8205/783/2/L35)

Table 2. Summary of model parameters and inferred results. ‘Tension’ refers to the statistical significance of the difference in the $\text{DM}_{\text{IGM}}-z$ relationships between FRBs in the ‘Pass’ and ‘NoPass’ groups. ‘Overdensity’ denotes the best-fit central baryonic overdensity (δ_0) in filaments.

model parameters				results	
galaxy stellar mass cut	persistence threshold	$R_{\text{ini}} [\text{Mpc}]$	$\sigma_{\text{DM}_{\text{IGM}}} [\text{pc cm}^{-3}]$	FRB number	central overdensity δ_0
$> 10^9 \text{M}_{\odot}$	5σ	2	60	37	21^{+13}_{-12}
				46	22^{+8}_{-8}
				26 ($z > 0.1$)	36^{+16}_{-17}
	5σ	2	100	34 ($z > 0.1$)	30^{+9}_{-9}
				37	24^{+20}_{-15}
				46	24^{+12}_{-11}
$> 10^{10} \text{M}_{\odot}$	5σ	2	60	37	37^{+36}_{-25}
				46	31^{+23}_{-20}
				37	25^{+11}_{-11}
	3σ	5	60	46	24^{+8}_{-7}
				37	13^{+7}_{-6}
				46	17^{+5}_{-6}
$> 10^{10} \text{M}_{\odot}$	5σ	2	60	37	49^{+19}_{-18}
	3σ	2	60	37	30^{+8}_{-9}

- Dey, A., Schlegel, D. J., Lang, D., et al. 2019, *AJ*, 157, 168, doi: [10.3847/1538-3881/ab089d](https://doi.org/10.3847/1538-3881/ab089d)
- Eckert, D., Jauzac, M., Shan, H., et al. 2015, *Nature*, 528, 105, doi: [10.1038/nature16058](https://doi.org/10.1038/nature16058)
- Faber, J. T., Ravi, V., Ocker, S. K., et al. 2024, arXiv e-prints, arXiv:2405.14182, doi: [10.48550/arXiv.2405.14182](https://doi.org/10.48550/arXiv.2405.14182)
- Fang, T., Marshall, H. L., Lee, J. C., Davis, D. S., & Canizares, C. R. 2002, *ApJL*, 572, L127, doi: [10.1086/341665](https://doi.org/10.1086/341665)
- Foreman-Mackey, D., Hogg, D. W., Lang, D., & Goodman, J. 2013, *PASP*, 125, 306, doi: [10.1086/670067](https://doi.org/10.1086/670067)
- Fukugita, M., Hogan, C. J., & Peebles, P. J. E. 1998, *ApJ*, 503, 518, doi: [10.1086/306025](https://doi.org/10.1086/306025)
- Galárraga-Espinoza, D., Langer, M., & Aghanim, N. 2022, *A&A*, 661, A115, doi: [10.1051/0004-6361/202141974](https://doi.org/10.1051/0004-6361/202141974)
- Galárraga-Espinoza, D., Cadiou, C., Gouin, C., et al. 2024, *A&A*, 684, A63, doi: [10.1051/0004-6361/202347982](https://doi.org/10.1051/0004-6361/202347982)
- Gordon, A. C., Fong, W.-f., Kilpatrick, C. D., et al. 2023, *ApJ*, 954, 80, doi: [10.3847/1538-4357/ace5aa](https://doi.org/10.3847/1538-4357/ace5aa)
- Haider, M., Steinhauser, D., Vogelsberger, M., et al. 2016, *MNRAS*, 457, 3024, doi: [10.1093/mnras/stw077](https://doi.org/10.1093/mnras/stw077)
- Heintz, K. E., Prochaska, J. X., Simha, S., et al. 2020, *ApJ*, 903, 152, doi: [10.3847/1538-4357/abb6fb](https://doi.org/10.3847/1538-4357/abb6fb)
- Huang, Y., Lee, K.-G., Libeskind, N. I., et al. 2025, *MNRAS*, 538, 2785, doi: [10.1093/mnras/staf417](https://doi.org/10.1093/mnras/staf417)
- Ibik, A. L., Drout, M. R., Gaensler, B. M., et al. 2023, arXiv e-prints, arXiv:2304.02638, doi: [10.48550/arXiv.2304.02638](https://doi.org/10.48550/arXiv.2304.02638)
- Ioka, K. 2003, *ApJL*, 598, L79, doi: [10.1086/380598](https://doi.org/10.1086/380598)
- James, C. W., Ghosh, E. M., Prochaska, J. X., et al. 2022, *MNRAS*, 516, 4862, doi: [10.1093/mnras/stac2524](https://doi.org/10.1093/mnras/stac2524)
- Khrykin, I. S., Ata, M., Lee, K.-G., et al. 2024, *ApJ*, 973, 151, doi: [10.3847/1538-4357/ad6567](https://doi.org/10.3847/1538-4357/ad6567)
- Law, C. J., Sharma, K., Ravi, V., et al. 2023, arXiv e-prints, arXiv:2307.03344, doi: [10.48550/arXiv.2307.03344](https://doi.org/10.48550/arXiv.2307.03344)
- Lee, K.-G., Khrykin, I. S., Simha, S., et al. 2023, *ApJL*, 954, L7, doi: [10.3847/2041-8213/acefb5](https://doi.org/10.3847/2041-8213/acefb5)
- Libeskind, N. I., van de Weygaert, R., Cautun, M., et al. 2018, *MNRAS*, 473, 1195, doi: [10.1093/mnras/stx1976](https://doi.org/10.1093/mnras/stx1976)
- Lorimer, D. R., Bailes, M., McLaughlin, M. A., Narkevic, D. J., & Crawford, F. 2007, *Science*, 318, 777, doi: [10.1126/science.1147532](https://doi.org/10.1126/science.1147532)
- Macquart, J. P., Prochaska, J. X., McQuinn, M., et al. 2020, *Nature*, 581, 391, doi: [10.1038/s41586-020-2300-2](https://doi.org/10.1038/s41586-020-2300-2)
- Malavasi, N., Aghanim, N., Douspis, M., Tanimura, H., & Bonjean, V. 2020, *A&A*, 642, A19, doi: [10.1051/0004-6361/202037647](https://doi.org/10.1051/0004-6361/202037647)
- Martizzi, D., Vogelsberger, M., Artale, M. C., et al. 2019, *MNRAS*, 486, 3766, doi: [10.1093/mnras/stz1106](https://doi.org/10.1093/mnras/stz1106)
- McQuinn, M. 2014, *ApJL*, 780, L33, doi: [10.1088/2041-8205/780/2/L33](https://doi.org/10.1088/2041-8205/780/2/L33)
- Migkas, K., Pacaud, F., Tuominen, T., & Aghanim, N. 2025, *A&A*, 698, A270, doi: [10.1051/0004-6361/202554944](https://doi.org/10.1051/0004-6361/202554944)
- Mo, J.-f., Zhu, W., & Feng, L.-L. 2025, *ApJS*, 277, 43, doi: [10.3847/1538-4365/adb616](https://doi.org/10.3847/1538-4365/adb616)
- Mo, J.-F., Zhu, W., Wang, Y., Tang, L., & Feng, L.-L. 2023, *MNRAS*, 518, 539, doi: [10.1093/mnras/stac3104](https://doi.org/10.1093/mnras/stac3104)
- Nevalainen, J., Tempel, E., Ahoranta, J., et al. 2019, *A&A*, 621, A88, doi: [10.1051/0004-6361/201833109](https://doi.org/10.1051/0004-6361/201833109)
- Nicastro, F., Mathur, S., Elvis, M., et al. 2005, *ApJ*, 629, 700, doi: [10.1086/431270](https://doi.org/10.1086/431270)
- Nicastro, F., Kaastra, J., Krongold, Y., et al. 2018, *Nature*, 558, 406, doi: [10.1038/s41586-018-0204-1](https://doi.org/10.1038/s41586-018-0204-1)
- O’Kane, C. J., Kuchner, U., Gray, M. E., & Aragón-Salamanca, A. 2024, *MNRAS*, 534, 1682, doi: [10.1093/mnras/stae2142](https://doi.org/10.1093/mnras/stae2142)
- Persic, M., & Salucci, P. 1992, *MNRAS*, 258, 14P, doi: [10.1093/mnras/258.1.14P](https://doi.org/10.1093/mnras/258.1.14P)
- Planck Collaboration, Ade, P. A. R., Aghanim, N., et al. 2016, *A&A*, 594, A13, doi: [10.1051/0004-6361/201525830](https://doi.org/10.1051/0004-6361/201525830)
- Popesso, P., Biviano, A., Marini, I., et al. 2024, arXiv e-prints, arXiv:2411.16555, doi: [10.48550/arXiv.2411.16555](https://doi.org/10.48550/arXiv.2411.16555)
- Prochaska, J. X., & Zheng, Y. 2019, *MNRAS*, 485, 648, doi: [10.1093/mnras/stz261](https://doi.org/10.1093/mnras/stz261)
- Prochaska, J. X., Macquart, J.-P., McQuinn, M., et al. 2019, *Science*, 366, 231, doi: [10.1126/science.aay0073](https://doi.org/10.1126/science.aay0073)
- Prochaska, J. X., Simha, S., almannin, et al. 2025,, v2.2 Zenodo, doi: [10.5281/zenodo.14804392](https://doi.org/10.5281/zenodo.14804392)
- Schaap, W. E., & van de Weygaert, R. 2000, *A&A*, 363, L29, doi: [10.48550/arXiv.astro-ph/0011007](https://doi.org/10.48550/arXiv.astro-ph/0011007)
- Shah, V., Shin, K., Leung, C., et al. 2025, *ApJL*, 979, L21, doi: [10.3847/2041-8213/ad9ddc](https://doi.org/10.3847/2041-8213/ad9ddc)
- Shannon, R. M., Bannister, K. W., Bera, A., et al. 2025, *PASA*, 42, e036, doi: [10.1017/pasa.2025.8](https://doi.org/10.1017/pasa.2025.8)
- Sharma, K., Ravi, V., Connor, L., et al. 2024, *Nature*, 635, 61, doi: [10.1038/s41586-024-08074-9](https://doi.org/10.1038/s41586-024-08074-9)
- Shin, K., Leung, C., Simha, S., et al. 2024, arXiv e-prints, arXiv:2410.07307, doi: [10.48550/arXiv.2410.07307](https://doi.org/10.48550/arXiv.2410.07307)
- Shull, J. M., Smith, B. D., & Danforth, C. W. 2012, *ApJ*, 759, 23, doi: [10.1088/0004-637X/759/1/23](https://doi.org/10.1088/0004-637X/759/1/23)
- Simha, S., Burchett, J. N., Prochaska, J. X., et al. 2020, *ApJ*, 901, 134, doi: [10.3847/1538-4357/abafc3](https://doi.org/10.3847/1538-4357/abafc3)
- Simha, S., Lee, K.-G., Prochaska, J. X., et al. 2023, *ApJ*, 954, 71, doi: [10.3847/1538-4357/ace324](https://doi.org/10.3847/1538-4357/ace324)
- Sousbie, T. 2011, *MNRAS*, 414, 350, doi: [10.1111/j.1365-2966.2011.18394.x](https://doi.org/10.1111/j.1365-2966.2011.18394.x)

- Sousbie, T., Pichon, C., & Kawahara, H. 2011, MNRAS, 414, 384, doi: [10.1111/j.1365-2966.2011.18395.x](https://doi.org/10.1111/j.1365-2966.2011.18395.x)
- Tanimura, H., Aghanim, N., Bonjean, V., Malavasi, N., & Douspis, M. 2020a, A&A, 637, A41, doi: [10.1051/0004-6361/201937158](https://doi.org/10.1051/0004-6361/201937158)
- Tanimura, H., Aghanim, N., Douspis, M., & Malavasi, N. 2022, A&A, 667, A161, doi: [10.1051/0004-6361/202244158](https://doi.org/10.1051/0004-6361/202244158)
- Tanimura, H., Aghanim, N., Kolodzig, A., Douspis, M., & Malavasi, N. 2020b, A&A, 643, L2, doi: [10.1051/0004-6361/202038521](https://doi.org/10.1051/0004-6361/202038521)
- Tanimura, H., Hinshaw, G., McCarthy, I. G., et al. 2019, MNRAS, 483, 223, doi: [10.1093/mnras/sty3118](https://doi.org/10.1093/mnras/sty3118)
- Tendulkar, S. P., Bassa, C. G., Cordes, J. M., et al. 2017, ApJL, 834, L7, doi: [10.3847/2041-8213/834/2/L7](https://doi.org/10.3847/2041-8213/834/2/L7)
- Tuominen, T., Nevalainen, J., Tempel, E., et al. 2021, A&A, 646, A156, doi: [10.1051/0004-6361/202039221](https://doi.org/10.1051/0004-6361/202039221)
- van de Weygaert, R., & Schaap, W. 2009, in Data Analysis in Cosmology, ed. V. J. Martínez, E. Saar, E. Martínez-González, & M. J. Pons-Bordería, Vol. 665, 291–413, doi: [10.1007/978-3-540-44767-2_11](https://doi.org/10.1007/978-3-540-44767-2_11)
- Vikhlinin, A., Kravtsov, A., Forman, W., et al. 2006, ApJ, 640, 691, doi: [10.1086/500288](https://doi.org/10.1086/500288)
- Yamasaki, S., & Totani, T. 2020, ApJ, 888, 105, doi: [10.3847/1538-4357/ab58c4](https://doi.org/10.3847/1538-4357/ab58c4)
- Yang, K. B., Wu, Q., & Wang, F. Y. 2022, ApJL, 940, L29, doi: [10.3847/2041-8213/aca145](https://doi.org/10.3847/2041-8213/aca145)
- Yang, Q.-R., Zhu, W., Yu, G.-Y., et al. 2025, ApJ, 989, 187, doi: [10.3847/1538-4357/adea3](https://doi.org/10.3847/1538-4357/adea3)
- Yang, X., Xu, H., He, M., et al. 2021, ApJ, 909, 143, doi: [10.3847/1538-4357/abddb2](https://doi.org/10.3847/1538-4357/abddb2)
- Yao, J. M., Manchester, R. N., & Wang, N. 2017, ApJ, 835, 29, doi: [10.3847/1538-4357/835/1/29](https://doi.org/10.3847/1538-4357/835/1/29)
- Zhang, B. 2023, Reviews of Modern Physics, 95, 035005, doi: [10.1103/RevModPhys.95.035005](https://doi.org/10.1103/RevModPhys.95.035005)
- Zhang, G. Q., Yu, H., He, J. H., & Wang, F. Y. 2020, ApJ, 900, 170, doi: [10.3847/1538-4357/abaa4a](https://doi.org/10.3847/1538-4357/abaa4a)
- Zhu, W., & Feng, L.-L. 2017, ApJ, 838, 21, doi: [10.3847/1538-4357/aa61f9](https://doi.org/10.3847/1538-4357/aa61f9)
- Zhu, W., & Feng, L.-L. 2021, ApJ, 906, 95, doi: [10.3847/1538-4357/abcb90](https://doi.org/10.3847/1538-4357/abcb90)
- Zhu, W., Feng, L.-L., & Zhang, F. 2018, ApJ, 865, 147, doi: [10.3847/1538-4357/aadbb0](https://doi.org/10.3847/1538-4357/aadbb0)
- Zhu, W., Zhang, F., & Feng, L.-L. 2021, ApJ, 920, 2, doi: [10.3847/1538-4357/ac15f1](https://doi.org/10.3847/1538-4357/ac15f1)
- Zou, H., Gao, J., Zhou, X., & Kong, X. 2019, ApJS, 242, 8, doi: [10.3847/1538-4365/ab1847](https://doi.org/10.3847/1538-4365/ab1847)